An Ultrathin Single Crystalline Relaxor Ferroelectric Integrated on a High Mobility Semiconductor

Reza M. Moghadam[†], Zhiyong Xiao[‡], Kamyar Ahmadi-Majlan[†], Everett D. Grimley[§], Mark Bowden[∥], Phuong-Vu Ong[⊥], Scott A. Chambers[⊥], James M. Lebeau[§], Xia Hong[‡], Peter V. Sushko[⊥] and Joseph H. Ngai[†]*

[†]Department of Physics, University of Texas Arlington, Arlington, TX 76019, USA
[‡]Department of Physics and Astronomy, University of Nebraska Lincoln, Lincoln, NE 68588, USA
[§]Department of Materials Science and Engineering, North Carolina State University, Raleigh, NC 27695, USA
[∥]Environmental Molecular Sciences Laboratory, Earth & Biological Sciences Directorate, Pacific Northwest National Laboratory, Richland, WA 99352, USA
[⊥]Physical Sciences Division, Physical & Computational Sciences Directorate, Pacific Northwest National Laboratory, Richland, WA 99352, USA

ABSTRACT

The epitaxial growth of multifunctional oxides on semiconductors has opened a pathway to introduce new functionalities to semiconductor device technologies. In particular, the integration of gate materials that enable non-volatile or hysteretic functionality in field-effect transistors could lead to device technologies that consume less power, or allow for novel modalities in computing. Here we present electrical characterization of ultrathin single crystalline $SrZr_xTi_{1-x}O_3$ ($x = 0.7$) films epitaxially grown on a high mobility semiconductor, Ge. Epitaxial films of $SrZr_xTi_{1-x}O_3$ exhibit relaxor behavior, characterized by a hysteretic polarization that can modulate the surface potential of Ge. We find that gate layers as thin as 5 nm corresponding to an equivalent-oxide-thickness of just 1.0 nm exhibit a ~ 2 V hysteretic window in the capacitance-voltage characteristics. The development of hysteretic metal-oxide-semiconductor capacitors with nanoscale gate thicknesses opens new vistas for nanoelectronic devices.

KEYWORDS: Crystalline oxides on semiconductors, relaxor ferroelectrics, metal-oxide-semiconductor capacitors, multifunctional oxides

Ferroelectrics integrated on semiconductors have long been proposed to serve as a materials platform for a variety of electronic device technologies.[1,2] These proposed technologies envision utilizing the ferroelectric as a field-effect gate material in which its re-orientable polarization is coupled to itinerant carriers in a semiconducting channel. For applications in sensing, ferroelectric gate materials could lead to smart transistors that are sensitive to temperature and pressure.[3] In regards to computing, stabilization of the negative capacitance of ferroelectric gate materials could lead to field-effect transistors that require very little power to operate.[4] Ferroelectric gate materials could also lead to field-effect devices for non-volatile logic and memory due to the hysteretic component of polarization that persists after power is removed.[5] Such hysteretic devices could also be exploited in computing based on emerging neuromorphic architectures.[6] In short, a materials platform that combines ferroelectrics and semiconductors could lead to field-effect devices that far surpass the performance and functionality of present devices.

In this regard, advancements in thin film growth have enabled single crystalline ferroelectrics to be epitaxially integrated on semiconductors,[7] such as $Pb(Zr_{0.2}Ti_{0.8})O_3$ on Si,[8] $BaTiO_3/Ba_xSr_{1-x}TiO_3$ on Si,[9,10] $SrTiO_3$ on Si,[11] $BaTiO_3$ on GaAs[12] and $BaTiO_3$ on Ge.[13,14] Despite such progress, the development of scalable, metal-oxide-semiconductor (MOS) capacitors using single crystalline ferroelectric gate materials remains elusive. MOS capacitors enable the surface potential of a semiconductor to be modulated through an applied bias, and thus underpin the functionality of field-effect devices. Modulation of the surface potential gives rise to a change in the capacitance of the semiconducting electrode, which is manifested as dispersion in the capacitance-voltage (C-V) characteristics of a MOS capacitor. When the re-

orientable polarization of a ferroelectric gate material is coupled to the surface potential, hysteresis in the C-V characteristics emerges.[15] Realizing ferroelectric MOS capacitors is challenging for several reasons. First, coupling of the polarization of a ferroelectric to the surface potential of a semiconductor requires continuity in the electric displacement between materials that differ in elemental composition and bonding. Dangling bonds at interfaces between a ferroelectric and a semiconductor can trap charges that electrically screen the polarization. Second, a type-I arrangement in which the conduction (valence) band of the ferroelectric is above (below) the conduction (valence) band of the semiconductor is needed to enable ferroelectric MOS structures to function as capacitors.[16] Unfortunately, traditional ferroelectrics such as $BaTiO_3$ exhibit a type-II band alignment with respect to Si, Ge and GaAs, in which the conduction band of the oxide is below that of the semiconductor.[17,18] Third, for applications in computing, the continued lateral scaling of field-effect transistors places constraints on the thickness of gate materials that can be used in practical devices.[19,20] However, ferroelectricity is generally weakened with decreasing film thickness because of depolarization fields, which are strong for ferroelectrics grown on semiconductors due to longer screening lengths in the latter.[21] Due to the above difficulties, prior reports of single crystalline ferroelectric MOS capacitors have typically utilized thick ($\geq$ 90 nm) ferroelectric layers.[22,23]

Given the challenges of realizing MOS capacitors using conventional ferroelectrics, the investigation of other related materials is needed. Relaxors are a class of ferroelectrics that can be described by an ensemble of weakly interacting polar clusters, or polar nano-regions (PNRs).[24] In some relaxor systems, a ferroelectric state defined by the spontaneous emergence of long-range polarization at a temperature T_C occurs. In so-called canonical relaxors, though, spontaneous long-range polarization is not observed, and the PNRs enter a glass-like (termed

non-ergodic) regime at lower temperatures. A ferroelectric state can be achieved in some canonical relaxors even from within the non-ergodic regime through application of a sufficiently strong electric field.[25,26] Yet, even in the absence of a ferroelectric state,[27,28] applied-fields can re-orient PNRs to induce polarized states that persist for up to hours.[29,30] Such polarized states could offer non-volatile and hysteretic functionality in field-effect devices for applications.[31]

In this Letter, we present hysteretic MOS capacitors comprised of single crystalline $SrZr_xTi_{1-x}O_3$ $x = 0.7$ (SZTO) that has been grown on Ge, a semiconductor that is of interest for next-generation field-effect transistors due to its high carrier mobility. In standard ABO_3 perovskite structured relaxors, the origin of PNRs is linked to disorder in the composition of the B-site cation. In this regard, SZTO is similar to $BaZr_xTi_{1-x}O_3$, which is a relaxor that has been extensively characterized.[32] Unlike $BaZr_xTi_{1-x}O_3$ though, relaxor behavior has yet to be reported in bulk SZTO.[33] Here we show that relaxor behavior is observed in ultra-thin films of SZTO under compressive strain.[34] Capacitance measurements as a function of temperature reveal a pronounced peak that exhibits dispersion with frequency, consistent with the dielectric response of a canonical relaxor. Piezo-response force microscopy (PFM) measurements indicate that persistent domain structures can be written on the SZTO. Polarization-voltage (P-V) PUND characterization measures a hysteretic component of polarization that can modulate the surface potential of Ge, as revealed by C-V. Analysis of high angle annular dark-field (HAADF) images obtained through scanning transmission electron microscopy (STEM) reveals evidence for PNRs, namely, regions that exhibit non-centrosymmetric displacements of Ti/Zr cations.[24,35] *Ab initio* density functional theory (DFT) calculations indicate that non-centrosymmetric displacements of Ti cations substituted in a sublattice dominated by larger Zr cations play a key role in the formation of PNRs. We find that the field induced hysteretic polarization of SZTO is

robust, as 5 nm thick films corresponding to an equivalent-oxide-thickness (EOT) of just 1.0 nm exhibit a ~ 2 V wide hysteretic window in the C-V characteristics, opening a pathway to realize highly scalable non-volatile field-effect devices.

Epitaxial SZTO films 15 and 5 nm in thickness are grown on p-type Ge using oxide molecular beam epitaxy (MBE). As-grown films are electrically leaky, due to residual oxygen vacancies formed in the relatively low oxygen background pressure of the ultra-high vacuum MBE chamber. To minimize the presence of residual vacancies, the SZTO films are annealed *ex situ* in oxygen after growth. Thorough oxygenation of the SZTO films is achieved, as evidenced by the presence of a thin layer of GeO_x at the interface as shown in Figure S1 for the 15 nm thick film. The annealed films are compressively strained (a = 4.03 Å and c = 4.07 Å) relative to bulk SZTO of the same x = 0.7 Zr content (a = 4.048 Å and c = 4.052 Å),[36] as shown in Figure S2.

A signature of canonical relaxor behavior is the observation of a maximum in the dielectric constant ε at a temperature T_M, which disperses and is suppressed in magnitude with increasing probe frequency.[24,37] For our SZTO-Ge capacitors, capacitance measurements on a 15 nm thick film reveal a peak near T_M ~ 275 °C that disperses with temperature and is suppressed with frequency, as shown in Figure S3. The T_M that we observe is comparable to that of epitaxial thin films of $Pb(Mg_{1/3}Nb_{2/3})O_3$(90%)-$PbTiO_3$(10%) under compressive strain.[38]

PFM studies on the SZTO-Ge heterostructure were performed to characterize electric field induced domain structures. Figures 1a and 1b show spatial mappings of phase and amplitude response for a domain structure written on an as-annealed 15 nm thick film. Here, a conductive atomic-force-microscope (AFM) tip held at a bias of -10 V is used to write a rectangle, followed by an adjacent rectangle written at a tip bias of +10 V. The PFM data indicate that domain structures can be written on our SZTO-Ge heterostructures. The

topography, shown in Figure 1e, indicates that no irreversible electrochemical reactions occur on the surface due to poling. Figures 1c and 1d show the phase and amplitude responses, respectively, of the same region 48 hours after poling. For both polarization states, the time dependence of the PFM amplitude signal exhibit a fast relaxation within the initial 10 hours, which can be well characterized by a power-law dependence $T^{-\alpha}$ in which $\alpha = 0.22\pm0.01$ for the P_{up} state and 0.23±0.04 for the P_{down} state (Figure 1f). We note that the α 's we measure are consistent with those extracted from prior studies of strained $SrTiO_3$, which exhibits relaxor behavior.[30] After the initial relaxation, the domain structures are stabilized for at least 48 hours, which was the duration of the measurements.

We also characterized the switching dynamics of the film using piezo-response spectroscopy measurements, in which the tip is held in one location and the phase and amplitude response are measured as a function of applied bias. Figures 1g and 1h show the amplitude and phase responses of the tip, revealing ferroelectric butterfly-like hysteresis, and 180° phase shift, respectively. Note the arrows in Figure 1h denoting the counter-clockwise orientation of the hysteresis consistent with ferroelectric-like switching, as opposed to a clockwise orientation associated with charge injection that can also give rise to hysteresis.[39] Our measurements at various points across the surface show that the coercive voltage V_c ranges from ~ 1 to 2 V, indicating a coercive field E_c that ranges from 0.7 to 1.3 × 10^8 V/m. The latter is estimated via $E_c \sim V_c/15$ nm, which neglects the voltage drop in the Ge electrode. Such magnitudes for E_c are consistent with those observed in typical epitaxial ferroelectric thin films, which generally exhibit higher E_c's than bulk samples.[40,41] For example, E_c's ranging from ~ 2.5 – 3.1 × 10^8 V/m have been measured on thin films of $BaTiO_3$, which far exceeds the E_c in bulk (~ 0.25 × 10^8 V/m).[14] To facilitate discussion, we have used the terms coercive voltage and field, though it should

be noted that such terms do not necessarily have the same physical meaning for polarized states in relaxors in comparison to conventional ferroelectrics.[27] Asymmetry in the amplitude response is also observed, similar to that observed in epitaxial ferroelectric films that have asymmetric electrical/mechanical boundary conditions, e.g. a bottom electrode/substrate and a free surface. For example, asymmetry in the amplitude piezoresponse has been observed in ferroelectric films of $BaTiO_3$,[12,14] $PbTiO_3$,[42] and $PbZr_{0.8}Ti_{0.2}O_3$ (PZT).[43] The asymmetry in PFM amplitude is consistent with a preference for downwards polarization. The downwards polarization is so strong in some nanoscale regions that a -10 V tip bias is insufficient to switch the polarization upwards, as can be seen in Figure 1a-d. Regions that exhibit asymmetric coercive voltages that favor a downwards polarization are also observed in piezo-response spectroscopy measurements (not shown).

In contrast to traditional ferroelectrics, such as $BaTiO_3$, SZTO has a type-I band offset with respect to Ge, thus capacitors can be realized.[44,45] Capacitance-voltage measurements demonstrate that a hysteretic and re-orientable polarization in SZTO can be coupled to the surface potential of Ge. Figure 2a shows C-V characteristics of 15 nm thick SZTO taken between ± 3 V, ± 4 V and ± 5 V at 1 MHz. As expected for a MOS capacitor, dispersion in the capacitance with respect to applied voltage is observed, indicating modulation of the surface potential of Ge. Hysteresis emerges with an orientation with respect to the direction of the sweeping voltage that is consistent with switching of ferroelectric dipoles; thus, interface trap states are ruled out as the source of the hysteresis, as they induce hysteresis in the opposite direction.[15,46] Mobile ions also cannot account for the hysteresis observed in our capacitors, since a positive flat-band voltage is achieved, and the hysteresis does not diminish by increasing the rate at which the voltage is swept between positive and negative values, as shown in Figure S4a.[5]

Inversion can be achieved in our MOS capacitors, as shown by the low frequency C-V measurements in Figure S4b. The enhancement in hysteresis with magnitude of applied voltage is attributed to an increase in hysteretic polarization with electric field due to non-saturation in the polarization, which we further discuss below.

The type-I band offset of SZTO on Ge also enables the hysteretic component of polarization to be estimated. In general, P-V characterization using the Sawyer-Tower technique in capacitors with semiconducting electrodes (e.g., Si, Ge, GaAs) yields inaccurate measurements of the polarization, due to leakage currents that arise from the limited Schottky barrier height at the oxide-semiconductor interface.[13] For our SZTO-Ge capacitors, leakage currents are further enhanced due to the thinness of our SZTO films. The hysteretic component of the polarization, though, can be isolated from leakage currents using the PUND technique.[47,48] Here we define hysteretic component as being the polarization measured at zero applied field, i.e. akin to the remnant polarization measured in conventional ferroelectrics. Figure 2b shows the currents measured in response to switching P, N and non-switching U, D voltage ramps applied for positive and negative polarities to a Ni electrode. The magnitude of leakage current is larger for positive P, U voltage ramps in comparison to negative N, D voltage ramps, due to a difference in barrier height for charge injection.[13] A hysteretic component of polarization switching is clearly resolved, as excess current on the rising (falling) side of the switching P (N) voltage ramp is measured relative to the rising (falling) side of the non-switching U (D) ramp as shown in Figure 2b. Integration of the excess currents in P and N voltage ramps results in the two-respective polarization half-loops shown in Figure 2c. Note the different scales used for each polarization half-loop, as the amount of charge switched for positive polarity P ramp is larger than the charge for negative polarity N ramp. The difference in switching charge between P and

N polarities could be due to several factors. The leakage currents are large in comparison to the switching currents, rendering precise measurement of the latter difficult. Leakage currents that are a function of the polarization could also give rise to the observed difference.[13] Thus, we estimate the switching charge ranges from ~ 3 to 5.5 $\mu C/cm^2$, which corresponds to an approximate hysteretic polarization of ~ 2.2 $\mu C/cm^2$, for voltage ramps of ± 3 V on a 15 nm thick SZTO film. We find that the hysteretic polarization can be enhanced by increasing the magnitude of the voltage ramps, as shown in Figure S5 for PUND measurements taken between ± 4 V. Such non-saturated behavior in the polarization is often observed in thin-film relaxors.[27,28,49] Non-saturated polarization is also generally observed in conventional ferroelectrics integrated on semiconducting electrodes; examples include $SrBi_2Ta_2O_9$ on Si, $SrBi_2Ta_2O_9$ on GaAs, and even thick films of single crystalline $BaTiO_3$ on GaAs.[5,22,50,51] In terms of magnitude, the hysteretic polarization we measure in our SZTO films is comparable to or larger than the those of conventional ferroelectrics integrated on Si or GaAs electrodes.[5,22,51]

We find that the hysteretic and re-orientable polarization in SZTO grown on Ge is robust for films as thin as 5 nm. Figure 3a shows the C-V characteristics of 5 nm thick film taken between ± 3 V, which results in a 2 V wide hysteretic window. Domains can be written on the 5 nm thick SZTO films using PFM, as shown in the inset of Figure 3a, in which a tip bias of -7 V is applied to write a square, followed by a smaller interior square written with + 7 V. Interestingly, we find a stronger intrinsic downward polarization in the 5 nm thick SZTO in comparison to the 15 nm, prior to applying a field. An explanation for the enhanced downward polarization will be discussed below. Piezo-response spectroscopy also confirms butterfly-like hysteresis and 180° phase-shift in the amplitude and phase response, shown in Figure 3b and 3c, respectively. The annealed 5 nm thick SZTO films also exhibit relatively abrupt interfaces with

Ge, as shown in the HAADF STEM images in Figure 3d. An average ~ 0.6 nm thick layer of interfacial GeO_x is achieved with regions that even exhibit no discernible GeO_x (top panel) using our basic annealing set-up. In principle, more advanced techniques such as rapid thermal annealing should enable better control of the oxidation process to further minimize GeO_x. The 5 nm SZTO yields an EOT of 1.0 nm, which is approaching the EOT of gate oxides used in present conventional MOS transistors. Further study will be needed to understand how the interplay between strain, applied fields and screening charges in electrodes affects the free energy landscape of relaxors to stabilize polarized states in ultra-thin films.[35,52] In principle, the large hysteretic window in C-V achieved with an EOT of just 1.0 nm opens a pathway to realize highly scalable ferroelectric field-effect devices.

STEM imaging reveals evidence of non-uniform atom column displacements in unpoled films, the presence of which is consistent with PNRs. Spatial regions that exhibit non-centrosymmetric displacements of B-site cations relative to the A-site sub-lattice are a signature of PNRs in ABO_3 structured perovskites. To look for such displacements, mappings of the deviations of the Ti/Zr B-site atom columns from the ideal center of the perovskite cells bounded by their four neighboring A-site Sr atom columns are performed on HAADF images of a 5 nm thick film, as shown in Figure 3e. The directions of the arrows superimposed on the HAADF image represent the directions of the non-centrosymmetric Ti/Zr displacements, and the magnitude of the displacements are represented in color. A histogram summarizing displacements measured from several HAADF images is shown in Figure S6. The average magnitude in displacement is 6.5 ± 0.1 pm for SZTO and 4.2 ± 0.1 pm for Ge. Of the displacements measured, 6 % (0.5%) of Ti/Zr (Ge) displacements are greater than 15 pm. The measured Ti/Zr displacements are comparable to those measured in thin film $SrTiO_3$ exhibiting

relaxor behavior, where Ti sites in the nano-polar regions are found to displace by up to about 10 pm (predicted 6 pm average),[35] and with pure $PbTiO_3$ which has a mean Ti displacement of ~ 15 pm.[53] In contrast, the magnitudes and the directions of displacements are random in non-polar structures.[54] Mapping the deviation of a dumbbell from the center of its four neighboring dumbbells in the Ge substrate reveals uncorrelated smaller displacements, as shown in Figure 3e and Figure S7a-d.

Qualitative and semi-quantitative information on the correlation lengths of regions exhibiting Ti/Zr displacements can also be obtained from the HAADF images, which provides insight on the size of PNRs. Spatial correlation can be most easily seen in HAADF images in which the angular direction of the Ti/Zr displacements is represented in colored arrows, as shown in Figure S7c-d. We find that regions exhibiting correlated Ti/Zr displacements vary in size and shape, and typically range between ~ 1 to 5 nm, though larger (up to ~ 10 nm) have also been observed. The size of the observed regions are in good agreement with the theoretically calculated size of PNRs in $(Pb(Mg,Nb)O_3)_x(PbTiO_3)_{1-x}$,[55] and the size of PNRs experimentally measured in bulk specimens of $PbMg_{1/3}Nb_{2/3}O_3$.[56] The consistency between the correlation lengths measured in our films with the size of PNRs in bulk relaxors suggests that the preparation of STEM lamella process does not affect the size of PNRs. We note that our semi-quantitative analysis is limited by the thickness of the lamella, which is thicker than the average correlation length of displacements. Consequently, regions that may vary in alignment of Ti/Zr displacement along a given atom column are averaged. However, it is important to note that channeling and depth of focus of the electron probe results in a signal that is more strongly governed by the first few nanometers of material near the surface and the region within the depth

of focus.[57,58] Consequently, the Ti/Zr displacements in these regions dominate the overall measured displacement probed over the thickness of the lamella.

To gain insight on how PNRs form in strained SZTO thin films, we performed *ab initio* DFT modeling of this system. We first seek to understand the behavior of Ti cations substituted into a B-site sublattice dominated by Zr, as shown in Figure 4a. In pure $SrZrO_3$ (SZO) that is compressively strained to the lattice constant of Ge, all in-plane and out-of-plane Zr–O distances are 2.05 and 2.12 Å (see Figure 4b), respectively, indicating that bulk SZO does not exhibit lattice polarization even under compressive strain. In contrast, upon substituting a Ti atom into a Zr site, the out-of-plane Ti_{Zr}–O bond lengths split into short (1.92 Å) and long (2.16 Å) ones, as shown in Figure 4b (hollow squares). This effect is attributed to the smaller ionic radius of Ti^{4+} (74.5 pm) in comparison to Zr^{4+} (86 pm), which leads to a double-well potential energy surface for Ti^{4+} ions and, in turn, results in effectively 5-fold coordination of the Ti_{Zr} site. Importantly, the distortion of the Ti local environment induces disproportionation of Zr–O bond lengths into short (2.06 Å) and long (2.25 Å) ones at the neighboring Zr sites along the *c*-axis, (hollow squares in Figure 4b), which indicates that not only are Ti-centered octahedra polarized themselves, but they also polarize neighboring Zr-centered octahedra. We find that compressive strain enhances the magnitude of the polarization, though it does not induce the polarization *per se*.

To understand the cumulative effect of such displacements in a film which has random placement of Ti amongst a Zr sublattice, we consider 4 types of configurations of Ti cations, namely, column, screw, pairs and plane with an overall Ti concentration of 25%, as shown in Figure 4c. The plane configuration was found to be energetically more favorable than the column (+0.1 eV) and the screw (+0.35 eV) configurations. However, given the small Ti to Zr ratio and

the substrate temperatures used during film growth, the predominance of planar structures is unlikely. The remaining configurations are within 0.25 eV (0.05 eV per Ti) from each other, and we propose that all of them are equally likely to be realized. A periodic, 2×2 lateral supercell slab is used to model the SZTO film on a $SrTiO_3$ substrate, as shown in Figure 4d, in which the in-plane lattice parameters are fixed to the experimental value of $a = b = 4.03$ Å, and the out-of-plane parameter is $c = 50.0$ Å. We choose $SrTiO_3$ (STO) as a substrate to bypass the complexities associated with modelling a SZTO/Ge interface with a partially oxidized GeO_x layer. In Figure 4e we plot the calculated bond lengths ΔZ along the *c*-axis between B-site (Ti,Zr) cations and oxygen anions located in adjacent planes. Each plane within the periodic slab is numbered as shown in Figure 4c. The colors indicate the different sets of the lateral fractional coordinates: black (0,0), red (1/2,0), green (0,1/2), blue (1/2,1/2) within the 2×2 lateral supercell. For example, black (0,0) in the column configuration would refer to the continuous chain of Ti cations along the *c*-axis shown in Figure 4c. If all Ti cations are situated in a single column along the *c*-axis, we find that a continuous sequence of short-long-short-long-etc., Ti–O bonds forms. If Ti cations are in different columns in a screw or pairs configuration, short-long Ti/Zr–O bond length sequences also form, though the difference in length between short and long bonds is smaller. Finally, for the plane configuration, long-long-short-short-long-long bond sequences appear that are locally symmetric with respect to the Ti plane.

The sequences of Ti/Zr–O bond lengths give rise to a dipole moment within each BO_2 plane. Figure 4f summarizes the out-of-plane contributions to polarization from each BO_2 plane for the 4 configurations (see Supporting Information for details on calculation). We note that in-plane components of polarization are also produced (not shown). The column configuration gives rise to a net polarization that is long-range, i.e. extends throughout the thickness of the

film, while screw, pairs and plane configurations lead to polarizations that are shorter in range and smaller in magnitude. These results also yield insight as to the predominance of a downward oriented polarization. The existence of the surface/vacuum interface gives rise to an asymmetry in the structure of the film and, accordingly, lattice polarization. Since Ti–O bonds are shorter than Zr–O bonds, Ti atoms in the top plane displace down with respect to the average Zr position in the same plane, and thus favors the short-long-short-… Ti/Zr–O bond pattern that corresponds to a downward polarization. As films becomes thinner, surface driven effects compete more strongly with the bulk in determining film properties. Thus, the PFM measurements indicating a stronger downward polarization in the 5 nm thick film compared to the 15 nm thick film prior to applying a field is consistent with this surface driven polarization effect predicted in our DFT. We note that within the 2 × 2 lateral cell used in our calculations, no surface reconstructions were observed. Aside from the dominant downward polarization at the surface, we find that the bulk corresponds to virtually zero net polarization because the statistical probability of distorted Ti/Zr-centered octahedra to contribute to upwards and downwards polarizations are the same everywhere except at the surface and the interface with the substrate. We note that many factors contribute to the formation, size, and dynamics of PNRs observed in relaxors, which lie beyond the scope of our *ab initio* model.[24] Nevertheless, our calculations elucidate a key mechanism behind non-centrosymmetric cation displacements in SZTO that can prompt the formation of PNRs.

Similar to other relaxor materials, the dynamics of PNRs in our SZTO films is complicated, as indicated by evidence for multiple relaxation times and static PNRs in the PFM.[59,60] While the PFM, PUND and C-V clearly indicate a polarized state can be induced in SZTO through an applied field, a question to be addressed is whether a long-range ferroelectric

state can be achieved. On the one hand, the persistence of written domains for days is consistent with ferroelectricity. On the other hand, saturation in the P-V characteristics has yet to be observed, which would provide more compelling evidence of ferroelectricity. However, as noted, even conventional ferroelectrics integrated on semiconducting electrodes (e.g. Si, GaAs) seldom exhibit saturated P-V characteristics.[5,22,51] Complementary studies of SZTO thin film capacitors using metallic electrodes could yield further insight in this regard.

In summary, we have realized MOS capacitors exhibiting ~ 2 V wide hysteretic C-V characteristics using 5 nm thick single crystalline SZTO, corresponding to an EOT of just ~ 1 nm. Through the epitaxial growth of SZTO on Ge, we have achieved continuity in the electric displacement, a type-I band offset, and a re-orientable polarization at nanoscale film thicknesses. The manipulation of PNRs in thin films of SZTO on Ge demonstrates how epitaxial strain, reduced dimensionality and applied electric fields can be exploited to realize technologically important behavior in multifunctional oxides. The realization of MOS capacitors exhibiting hysteretic functionality using nanoscale thick gate materials opens new vistas for nanoelectronic devices. Here we have shown that relaxors are promising materials for such applications, and thus warrant further study and development.

Methods. *Film growth.* Crystalline SZTO films were grown on p-type Ge (100) wafers (AXT Inc., $\rho \approx 0.02$ Ωcm) using reactive MBE in a custom-built chamber operating at a base pressure of $< 2 \times 10^{-10}$ Torr. The Ge wafers were introduced into the growth chamber after an etch and oxidation process that involved repeated dips in diluted HCl and H_2O_2. A clean dimerized Ge surface was obtained by thermally desorbing the resulting GeO_2 from the surface in ultra-high vacuum at ~ 600 °C. The Ge wafer was then cooled to ~ 400 °C at which a half monolayer (ML)

of Sr metal was deposited to passivate the clean Ge surface. Thermal effusion cells (Veeco and SVT Associates) were used to evaporate all source metals for growth, and fluxes were calibrated using a quartz crystal monitor (Inficon). The Ge wafer was then cooled to room temperature at which an additional 1 ML of SrO was deposited, followed by co-deposition of 1.5 ML of SrO and 2 monolayers of $Zr_xTi_{1-x}O_2$ in an oxygen background pressure of 3×10^{-7} Torr. The temperature of each effusion cell was adjusted to control the relative flux rates of the metal sources to achieve the desired Sr, Ti and Zr ratios and enable co-deposition. The Ge was then heated to ~ 550 °C to crystallize the 2.5 unit-cells of SZTO. Subsequent SZTO layers were grown 3 unit-cells at a time through co-deposition of Sr, Ti and Zr fluxes at a substrate temperature of ~ 250 °C, and background oxygen pressure of 3×10^{-7} Torr. The substrate temperature was increased to ~ 580 °C in ultra-high-vacuum after each 3 unit-cells deposition of SZTO to improve crystallinity.

Postgrowth annealing. Both 15 nm and 5 nm thick SZTO films were annealed in a tube furnace (MTI corp.) at ambient pressures in flowing ultrapure oxygen that had been bubbled through high purity deionized water. Films were inserted into the tube furnace that was preset to a temperature of 400 °C, as measured by the thermocouple in the furnace. The data presented in this paper was for 20 minutes of annealing for the 15 nm thick SZTO and 5 minutes for the 5 nm thick SZTO.

Piezo-response force Microscopy. The polarization writing, switching hysteresis loop and time-dependence piezo-response amplitude study of SZTO films on Ge were studied at room temperature with a Bruker multimode 8 AFM working in the contact mode, with a small AC voltage applied to a conductive tip and the substrate grounded, or vice versa (SCM-PIT). Measurements were performed at frequencies close to the cantilever resonance (~300 kHz) with

a bias voltage of 200-500 mV, to eliminate any spurious artifacts due to ion migration.[61] To measure the PFM switching hysteresis, we first applied a DC voltage pulse V_{bias} with a typical time period of t_{pulse} = 100 ms, and then measure the PFM response after the removal of the DC bias for a wait time of t_{wait} = 100 ms. The bias-off technique allows us to eliminate the electrostatic artifact associated with the DC tip bias.[62]

Capacitance-Voltage and Polarization-Voltage measurements. 30 nm thick Ni electrodes ranging in diameter from 20 μm to 270 μm were deposited through a shadow mask using electron beam evaporation. The backsides of the Ge wafers were mechanically scratched and InGa eutectic was applied to form a counter electrode. The C-V and P-V characterizations were performed on a probe station using flexible probe whiskers. An Agilent 4284A LCR meter was used for the C-V measurements. A Radiant II ferroelectric tester was used for the PUND measurements. For the PUND measurement, each junction was measured 30 times and the data was averaged to improve signal to noise.

Capacitance versus temperature measurements. The capacitance versus temperature measurements were performed on a heated stage situated on a probe station equipped with flexible, probe whiskers and an Agilent 4284A LCR meter. An 11 mV AC probe signal was used in conjunction with a DC voltage of -0.3 V, which biased the SZTO-Ge heterojunction towards accumulation. A wafer with electrodes deposited on top was broken into pieces. A separate piece was used for each frequency measurement, in which each piece was cycled from room to high temperature only once.

Scanning Transmission Electron Microscopy. STEM lamella were prepared using conventional wedge polishing with an Allied Multiprep followed by Ar + ion milling using a Fischione Model 1050, where final milling voltages were 500 V or less, and where in some cases

liquid nitrogen was used to cool the sample stage during milling. Samples were capped with Ni to protect the films during preparation. HAADF-STEM was conducted on a probe-corrected FEI Titan G2 60 – 300 kV operated at 200 kV with a detector inner semi-angle of approximately 77 mrad, and probe semi-convergence angles of either 13.5 or 19.6 mrad. Due to relative beam sensitivity of SZTO, beam currents of 60 pA or lower were used. STEM images were acquired utilizing the RevSTEM acquisition method to remove thermal drift related image distortion.[63] Acquisition parameters included using 20 to 40 1024 pix × 1024 pix image frames recorded with 2 μs/pix dwell time and a 90° rotation of the scan coordinates between each successive image. In the case of the 5 nm thick SZTO film samples used for lattice parameter measurements, global residual distortion was removed using images of an Si substrate acquired during the same microscope session.[64] In these images, atom column locations were isolated and indexed.[65] A Gaussian template was used to fit the atom columns in the 5 nm thick films of SZTO, whereas either a Gaussian template or a <110> dumbbell template was used to fit the locations of the Ge dumbbells. SZTO and Ge lattice parameters were taken from the same images, and are presented (see Supporting Information) as the mean and standard error of measurements of four different images acquired from different sample regions and thicknesses, and even from different lamella. The Ge unit cells closest to the interface with SZTO were excluded from the Ge lattice parameter measurement. The deviations of an atom column were determined by taking the difference between the ideal position (the mean position of its four nearest neighbors, which is the cell center) and the measured position. GeO_x layer thicknesses were measured as the distances between corresponding inflection points in the second derivative of integrated line profiles taken from non-RevSTEM images. SZTO film thicknesses were measured using the same method and images for comparison (see Supporting Information). These measurements were averaged over

images acquired from different lamella regions and thicknesses.

Density Functional Theory Calculations. For the bulk calculation, we consider a SZO 2×2×2 supercell and optimized the *c*-axis lattice parameter with the in-plane lattice parameters fixed at the experimental value of the annealed SZTO films. With the lattice parameters fixed, we then optimize the internal coordinates for a Ti concentration of 12.5%, as shown in Figure 4a. For the SZTO/STO slab, the STO and SZTO parts of the system are three- and five-unit-cell thick, respectively, and a 2×2 lateral supercell is used with the in-plane lattice parameters fixed at the experimental value corresponding to the annealed SZTO films supported on Ge ($a = b =$ 4.03 Å) and the out-of-plane parameter $c = 50.0$ Å. The distance between the top and the bottom planes of the slab was under 30 Å, leaving the vacuum gap of at least 20 Å. The total energy of the system was minimized with respect to all degrees of freedom of the SZTO part of the slab and out-of-plane degrees of freedom of the atoms in the three unit-cell thick STO part; the in-plane coordinates of atoms of the STO part and the SrO plane at the bottom of the slab were fixed to mimic substrate-induced constraints, as indicated in Figure 4d. The calculations were performed using the Vienna Ab Initio Simulation Package (VASP).[66,67] The projected augmented wave method was used to approximate the electron-ion potential.[68] Exchange-correlation effects were treated within the Perdew-Burke-Ernzerhof functional form of the generalized gradient approximation, modified for solids (PBEsol).[69] A plane-wave basis with a 500 eV cutoff and a 2×2×1 and 2×2×2 Monkhorst-Pack k-point meshes were used for the SZTO slab and bulk, respectively. The charge and spin density distributions were analyzed using the Bader method.[70] The energies of self-consistent calculations were converged to 10^{-5} eV/cell. The method for determining the layer-resolved polarization is discussed in the Supporting Information.

ASSOCIATED CONTENT

Further information on the structural, and electrical characterization of the SZTO films as well as model calculations can be found in the **Supporting Information**.

AUTHOR INFORMATION

Corresponding Author

*Email: jngai@uta.edu

Author Contributions

R. M. M. was responsible for the annealing of samples and X-ray diffraction, C-V and P-E characterizations. Z. X. and X. H. were responsible for the PFM characterization. K. A. M. was responsible for sample growth. E. D. G. and J. M. L. were responsible for STEM characterization. M. B. and S. A. C. were responsible for the X-ray direct-space mapping. P. -V. O., S. A. C. and P. V. S. were responsible for the DFT calculations. J. H. N. was responsible for overall direction of investigation. The manuscript was written with contributions from all authors. All authors have given approval to the final version of the manuscript.

Notes

The authors declare no competing financial interests.

ACKNOWLEDGMENT

This work was supported by National Science Foundation (NSF) under award No. DMR-1508530. The work performed at the University of Nebraska was supported by DOE (BES) Award DE-SC0016153 funded by the U.S. Department of Energy, Office of Basic Energy

Sciences for the scanning probe studies. The work performed at North Carolina State University was supported by the NSF under award No. DMR-1350273. E.D.G. acknowledges support for this work through a National Science Foundation Graduate Research Fellowship (Grant DGE-1252376). This work was performed in part at the Analytical Instrumentation Facility (AIF) at North Carolina State University, which is supported by the State of North Carolina and the National Science Foundation (award number ECCS-1542015). The AIF is a member of the North Carolina Research Triangle Nanotechnology Network (RTNN), a site in the National Nanotechnology Coordinated Infrastructure (NNCI). DFT, and x-ray diffraction performed at Pacific Northwest National Laboratory was supported by the U.S. Department of Energy, Office of Science, Division of Materials Sciences and Engineering under Award #10122. The PNNL work was performed in the Environmental Molecular Sciences Laboratory, a national scientific user facility sponsored by the Department of Energy's Office of Biological and Environmental Research and located at PNNL.

REFERENCES

(1) Dawber, M.; Rabe, K. M.; Scott, J. F. *Rev. Mod. Phys.* **2005**, *77*, 1083-1130.

(2) Hong, X. *J. Phys.: Condens. Matter* **2016**, *28*, 103003.

(3) Wu, Y. –R.; Singh, J. *IEEE Trans. Electron. Dev.* **2005**, *52*, 284-293.

(4) Khan, A. I.; Chatterjee, K.; Wang, B.; Drapcho, S.; You, L.; Serrao, C.; Bakaul, S. R.; Ramesh, R.; Salahuddin, S. *Nat. Mater.* **2014**, *14*, 182-186.

(5) Han, J. –P.; Ma, T. P. *App. Phys. Lett.* **1998**, *72*, 1185-1186.

(6) *Neuromorphic Computing: From Materials to Systems Architecture*; U.S. Department of Energy, 2016.

(7) McKee, R. A.; Walker, F. J.; Chisholm, M. F. *Phys. Rev. Lett.* **1998**, *81*, 3014-3017.

(8) Lin, A.; Hong, X.; Wood, V.; Verevkin, A. A.; Ahn, C. H.; McKee, R. A.; Walker, F. J.; Specht, E. D. *Appl. Phys. Lett.* **2001**, *78*, 2034-2036.

(9) Vaithyanathan, V.; Lettieri, J.; Tian, W.; Sharan, A.; Vasudevarao, A.; Li, Y. L.; Kochhar, A.; Ma, H.; Levy, J.; Zschack, P.; et al. *J. Appl. Phys.* **2006**, *100*, 024108.

(10) Dubourdieu, C.; Bruley, J.; Arruda, T. M.; Posadas, A.; Jordan-Sweet, J.; Frank, M. M.; Cartier, E.; Frank, D. J.; Kalinin, S. V.; Demkov, A. A.; et al. *Nat. Nanotech.* **2013**, *8*, 881-881.

(11) Warusawithana, M.; Cen, C.; Sleasman, C. R.; Woicik, J. C.; Li, Y.; Kourkoutis, L.; Klug, J. A.; Li, H.; Ryan, P.; Wang, L. -P.; et al. *Science* **2009**, *324*, 367-370.

(12) Contreras-Guerrero, R.; Veazey, J.; Levy, J.; Droopad, R. *Appl. Phys. Lett.* **2013**, *102*, 012907.

(13) Ngai, J. H.; Kumah, D. P.; Ahn, C. H.; Walker, F. J. *Appl. Phys. Lett.* **2014**, *104*, 062905.

(14) Ponath, P.; Fredrickson, K.; Posadas, A. B.; Ren, Y.; Wu, X.; Vasudevan, R. K.; Okatan, M. B.; Jesse, S.; Aoki, T.; McCartney, M. R.; et al. *Nat. Comm.* **2015**, *6*, 6067.

(15) Miller, S. L.; McWhorter, P. J. *J. Appl. Phys.* **1992**, *72*, 5999-6010.

(16) Rossel, C.; Mereu, B.; Marchiori, C.; Caimi, D.; Sousa, M.; Guiller, A.; Siegwart, H.;

Germann, R.; Locquet, J. –P.; Fompeyrine, J.; et al. *Appl. Phys. Lett.* **2006**, *89*, 053506.

(17) Amy, F.; Wan, A.; Kahn, A.; Walker, F. J.; McKee, R. A. *J. Appl. Phys.* **2004**, *96*, 1635-1639.

(18) Chambers, S. A.; Liang, Y.; Yu, Z.; Droopad, R.; Ramdani, J. *J. Vac. Sci. Technol. A* **2001**, *19*, 934-939.

(19) Cheng, B.; Cao, M.; Rao, R.; Inani, A.; Voorde, P. V.; Greene, W. M.; Stork, J. M.;Yu, Z.; Zeitzoff, P. M.; Woo, J. C. *IEEE Trans. Electron Devices* **1999**, *46*, 1537-1544.

(20) Liang, P.; Jiang, J.; Song, Y. *J. Phys. D: Appl. Phys.* **2008**, *41*, 215109.

(21) Reiner, J. W.; Walker, F. J.; McKee, R. A.; Billman, C. A.; Junquera, J.; Rabe, K. M.; Ahn, C. H. *Phys. Stat. Solidi B* **2004**, *241*, 2287-2290.

(22) Murphy, T. E.; Chen, D.; Phillips, J. D. *Appl. Phys. Lett.* **2004**, *85*, 3208-3210.

(23) Niu, G.; Yin, S.; Saint-Girons, G.; Gautier, B.; Lecoeur, P.; Pillard, V.; Hollinger, G.; Vilquin, B. *Microelectron. Eng.* **2011**, *88*, 1232-1235.

(24) Bokov, A. A.; Ye, Z. –G. *J. Mater. Sci.* **2006**, *41*, 31-52.

(25) Colla, E. V.; Koroleva, E. Y.; Okuneva, N. M.; Vakhrushev, S. B. *Phys. Rev. Lett.* **1995**, *74*, 1681-1684.

(26) Dkhil, B.; Kiat, J. *J. Appl. Phys.* **2001**, *90*, 4676-4681.

(27) Tyunina, M.; Pintilie, I.; Iuga, A.; Pintilie, L. *Phys. Rev. B* **2014**, *89*, 094106.

(28) Tyunina, M.; Pintilie, I.; Iuga, A.; Stratulat, M. S.; Pintilie, L. *J. Phys.: Condens. Matter* **2014**, *26*, 325901.

(29) Shvartsman, V. V.; Kholkin, A. L.; Tyunina, M.; Levoska, J. *Appl. Phys. Lett.* **2005**, *86*, 222907.

(30) Jang, H. W.; Kumar, A.; Denev, S.; Biegalski, M. D.; Maksymovych, P.; Bark, C. W.; Nelson, C. T.; Folkman, C. M.; Baek, S. H.; Balke, N.; et al. *Phys. Rev. Lett.* **2010**, *104,* 197601.

(31) Hoffman, J.; Pan, X.; Reiner, J. W.; Walker, F. J.; Han, J. P.; Ahn, C. H.; Ma, T. P. *Adv. Mater.* **2010**, *22*, 2957-2961.2957-2961, 2010.

(32) Maiti, T.; Guo, R.; Bhalla, A. S. *Ferroelectrics* **2011**, *425*, 4-26.

(33) Tsurumi, T.; Teranishi, T.; Wada, S.; Kakemoto, H.; Fukunaga, O.; Nakada, M.; Akedo, J. *J. Ceram. Soc. Jpn.* **2006**, *114*, 774-781.

(34) Prosandeev, S.; Wang, D.; Bellaiche, L. *Phys. Rev. Lett.* **2013**, *111*, 247602.

(35) Lee, D.; Lu, H.; Gu, Y.; Choi, S. –Y.; Li, S.; Ryu, S.; Paudel, T. R.; Song, K.; Mikheev, E.; Lee, S.; et al. *Science* **2015**, *349*, 1314-1317.

(36) Wong, T. K. –Y.; Kennedy, B. J.; Howard, C. J.; Hunter, B. A.; Vogt, T. *J. Sol. Stat. Chem.* **2001**, *156*, 255-263.

(37) Tu, C. –S.; Chen, L. –F.; Schmidt, V. H.; Tsai, C. –L. *Jpn. J. Appl. Phys.* **2001**, *40*, 4118-4125.

(38) Nagarajan, V.; Ganpule, C. S.; Nagaraj, B.; Aggarwal, S.; Alpay, S. P.; Roytburd, A. L.; Williams, E. D.; *Appl. Phys. Lett.* **1999**, *75*, 4183-4185.

(39) Vasudevan, R.; Balke, N.; Maksymovych, P.; Jesse, S.; Kalinin, S. V. 2017, *arXiv:1701.01128,* accessed 07/11/2017.

(40) Kay, H. F.; Dunn, J. W. *Phil. Mag.* **1962**, *7*, 2027-2034.

(41) Dawber, M.; Chandra, P.; Littlewood, P. B; Scott, J. F. *J. Phys.: Condens. Matter* **2003**, *15*, L393-L398.

(42) Lichtensteiger, C.; Dawber, M.; Stucki, N.; Triscone, J.; Hoffman, J.; Yau, J.; Ahn, C.; Despont, L.; Aebi, P. *Appl. Phys. Lett.* **2007**, *90*, 052907.

(43) Chen, J.; Lu, H.; Liu, H. –J.; Chu, Y. –H.; Dunn, S.; Ostrikov, K.; Gruverman, A.; Valanoor, N. *Appl. Phys. Lett.* **2013**, *102*, 182904.

(44) Jahangir-Moghadam, M.; Ahmadi-Majlan, K.; Shen, X.; Droubay, T.; Bowden, M.; Chrysler, M.; Su, D.; Chambers, S.; Ngai, J. H. *Adv. Mater. Interfaces* **2015**, *2*, 1400497.

(45) Kajdos, A. P.; Ouellette, D. G.; Cain, T. A.; Stemmer, S. *Appl. Phys. Lett.* **2013**, *103*, 082120

(46) Nicollian, E. H.; Brews J. R. *MOS Physics and Technology*; John Wiley& Sons: New York, NY, 1986.

(47) Scott, J. F.; Kammerdiner, L.; Parris, M.; Traynor, S.; Ottenbacher, V.; Shawabkeh, A.; Oliver, W. F. *J. Appl. Phys.* **1988**, *64*, 787-792.

(48) Fukunaga, M.; Noda, Y. *J. Phys. Soc. Jpn.* **2008**, *77*, 064706.

(49) Lewczuk, U.; Suchanicz, J.; Karpierz, M.; Stachowski, G. *Phase Trans.* **2016**, *90*, 60-64.

(50) Liu, X. H.; Liu, Z. G.; Wang, Y. P.; Zhu, T.; Liu, J. M. *Appl. Phys. A* 2003, *76*, 197-199.

(51) Huang, W.; Wu, Z. P.; Hao, J. H. *Appl. Phys. Lett.* **2009**, *94*, 032905.

(52) Guzman-Verri, G. G.; Littlewood, P. B.; Varma, C. M., *Phys. Rev. B* **2013***,* 88, 134106.

(53) Glazer, A. M.; Mabud, S. A. *Acta Crystallogr. Sect. B Struct. Crystallogr. Cryst. Chem.* **1978***,* 34, 1065-1070.

(54) Sang, X.; Grimley, E. D.; Niu, C.; Irving, D.; LeBeau, J. M. *Appl. Phys. Lett.* **2015**, *106*, 061913.

(55) Takenaka, H.; Grinberg ,I.; Liu, S.; Rappe, A. M. *Nature* **2017**, 546, 391-395.

(56) Xu, G.; Shirane, G.; Copley, J. R. D.; Gehring, P. M. *Phys. Rev. B* **2004***,* 69, 064112.

(57) Cosgriff, E. C.; Nellist, P. D. *Ultramicroscopy,* **2007**, 107, 626-634.

(58) Ishikawa, R.; Lupini, A. R.; Hinuma, Y.; Pennycook, S. J. *Ultramicroscopy,* **2015,** 151,122-129.

(59) Kholkin, A.; Morozovska, A.; Kiselev, D.; Bdikin, I.; Rodriguez, B.; Wu, P.; Bokov, A.; Ye, Z. –G.; Dkhil, B.; Chen, L. –Q.; et al. *Adv. Func. Mater.* **2011**, *21*, 1977-1987.

(60) Shvartsman, V. V.; Dkhil, B.; Kholkin, A. L. *Annu. Rev. Mater. Res.* **2013**, *43*, 423-449.

(61) Kumar, A.; Ciucci, F.; Morozovska, A.; Kalinin, S. V.; Jesse, S. *Nat. Chem.* **2011**, *3*, 707-713.

(62) Jesse, S.; Baddorf, A. P.; Kalinin, S. V. *Appl. Phys. Lett.* **2006**, *88*, 062908.

(63) Sang, X.; LeBeau, J. M. *Ultramicroscopy* **2014**, *138*, 28-35.

(64) Dycus, J. H.; Harris, J. S.; Sang, X.; Fancher, C. M.; Findlay, S. D.; Oni, A.; Chan, T.; Koch, C.; Jones, J.; Allen, L.; et al. *Microscopy and Microanalysis* **2015**, *21*, 946-952.

(65) Sang, X.; Oni, A. A.; LeBeau, J. M. *Microsc. Microanal.* **2014**, *20*, 1764-1771.

(66) Kresse, G.; Furthmüller, J. *Phys. Rev. B* **1996**, *54*, 11169-11186.

(67) Kresse, G.; Joubert, D. *Phys. Rev. B* **1999**, *59*, 1758-1775.

(68) Blöchl, P. E. *Phys. Rev. B* **1994**, *50*, 17953-17979.

(69) Perdew, J. P.; Ruzsinszky, A.; Csonka, G. I.; Vydrov, O. A.; Scuseria, G. E.; Constantin, L. A.; Zhou, X. L,; Burke, K. *Phys. Rev. Lett.* **2008**, *100*, 136406.

(70) Bader, R. *Atoms In Molecules - A Quantum Theory*; Clarendon Press: Oxford U.K , U.K, 1994.

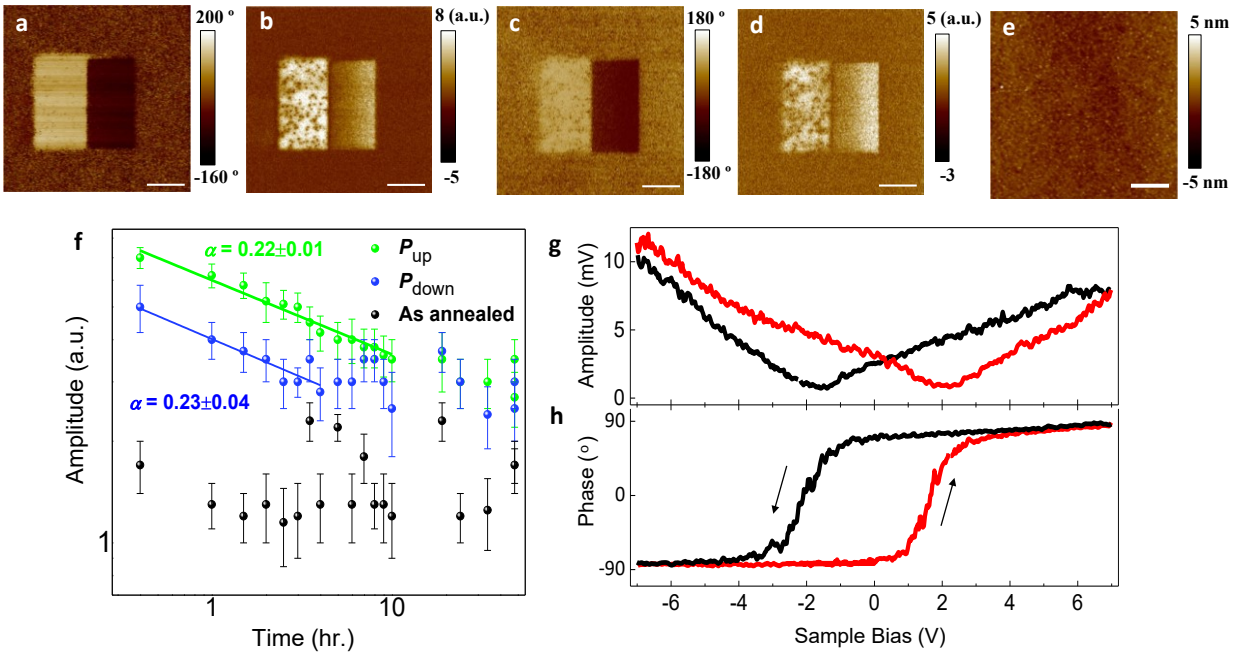

Figure 1. Piezo-response force microscopy of 15 nm thick SZTO film on Ge. (a) Phase and (b) amplitude response of domain structures 2.5 hours after writing. The lateral scale bar represents 2 µm. (c) Phase and (d), amplitude response of the same domain structures 48 hours after writing. (e) The topography of the film after domain writing, indicating no tip induced electrochemical changes on the surface. (f) Amplitude response as a function of time for P_{UP} and P_{DOWN} domain structures, and as-annealed parts of film surface. (g) Amplitude and (h), phase piezo-response taken in spectroscopy mode, showing butterfly-like hysteresis and 180° phase change, respectively.

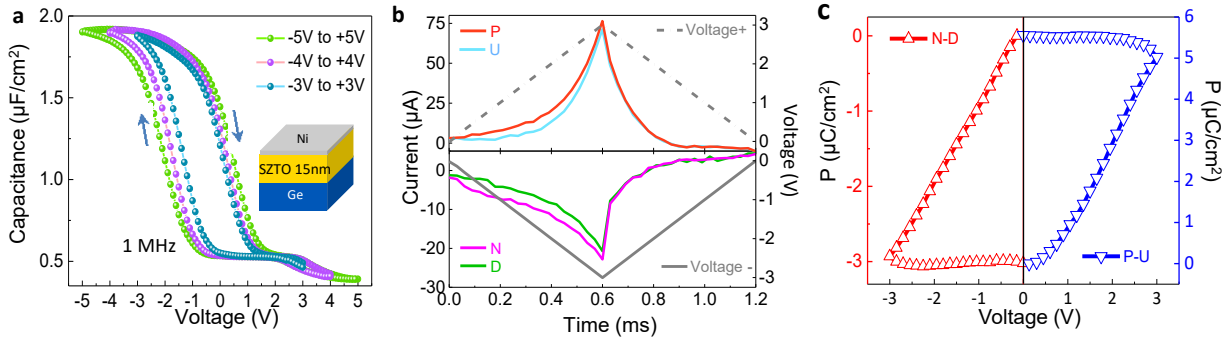

Figure 2. C-V and P-V characterization for 15 nm thick SZTO film on Ge. (a) C-V measurements showing hysteresis obtained for ± 3 V, ± 4 V and ± 5 V sweeps. (b) Currents measured from each voltage ramp of the PUND waveform plotted independently on the same time scale to enable comparison. Switching of the hysteretic component of ferroelectric polarization is observed as excess current is measured on the rising (falling) side of the switching P (N) voltage ramp relative to the rising (falling) side of the non-switching U (D) ramp, as shown in the upper (lower) panel. (c) P-V half-loops obtained by integrating switching currents from the PUND measurements taken using ± 3 V voltage ramps.

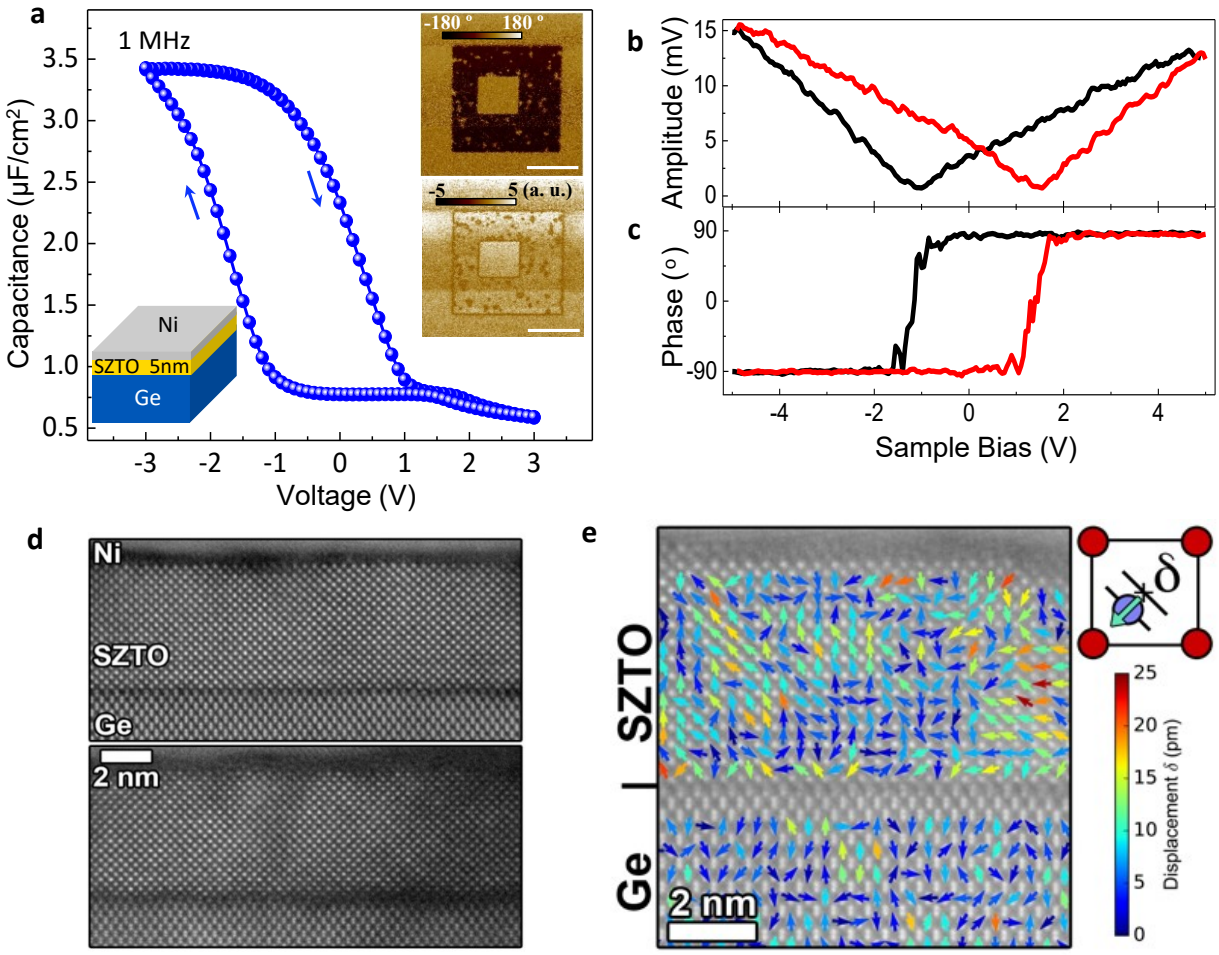

Figure 3. Electrical and structural characterization of 5 nm SZTO film on Ge. (a) C-V measurement of 5 nm thick SZTO film on Ge. Inset shows phase and amplitude contrast of domain structures written using PFM. Scale bar is 2 μm. (b) Amplitude and (c) phase piezo-response spectroscopy measurements of 5 nm thick SZTO on Ge. (d) HAADF STEM images taken on annealed 5 nm thick SZTO on Ge, showing relatively abrupt interfaces. Both images are from the same lamella, and show the variation of GeO_x formation at the interface, from little-to-no GeO_x in the top panel to containing regions around 0.5 nm thick as in portions of the bottom panel. (e) Magnitude and direction of non-centrosymmetric Ti/Zr column displacements δ superimposed on HAADF image of annealed 5 nm thick SZTO film on Ge. Top right schematic shows how δ is measured with respect to A-site and B-site cations. The color scale indicates the magnitudes of the displacements. Displacements clipped to 25 pm in the image to spread the color range.

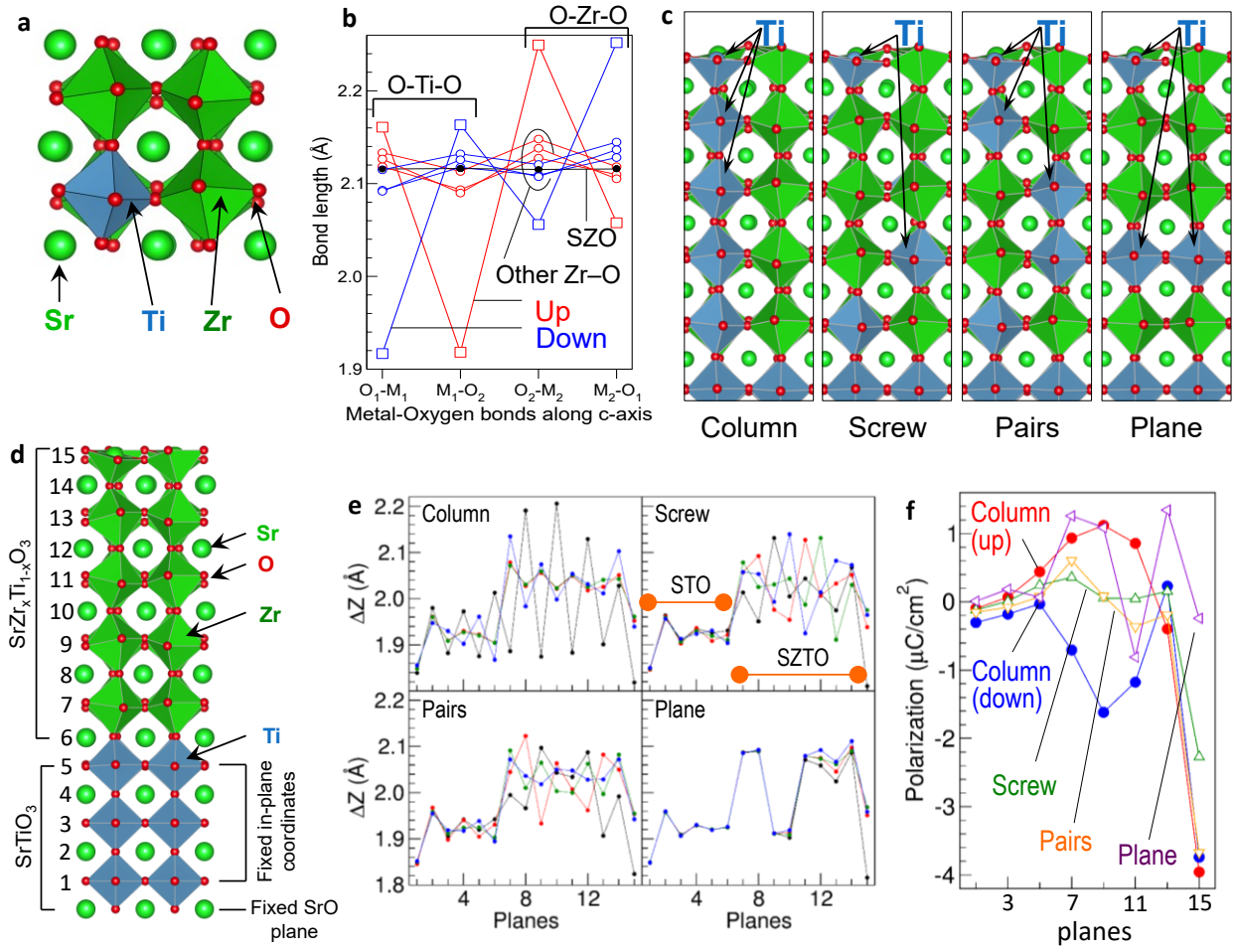

Figure 4. Density functional theory of SZTO. (a) Structure of the bulk SZTO with Ti concentration of 12.5% as obtained using the 2×2×2 supercell subjected to compressive strain. (b) Metal-oxygen distances in O–(Zr,Ti)–O chains along the *c*-axis show that polarization of Ti-centered octahedra induces similar polarization of Zr-centered octahedra. (c) DFT modelling of SZTO film with various configurations of Ti distributions, namely, column, screw, pairs and plane. (d) Periodic, 2×2 lateral supercell used to model SZTO film on a $SrTiO_3$ substrate (Ti dopants are not shown). Numbers on the left denote planes. (e) Separation (ΔZ) between *B*-site (Ti,Zr) cations and Oxygen anions situated in adjacent planes, stacked along the *c*-axis for the various distributions of Ti shown in (c). Colors indicate the different sets of the lateral fractional coordinates: black (0,0), red (1/2,0), green (0,1/2), blue (1/2,1/2) within the 2×2 lateral supercell. (f) The resulting unit-cell resolved out-of-plane component of polarization due to Ti and Zr cation displacements for each of the Ti configurations.